Vortex-induced vibration prediction of a flexible cylinder by three-dimensional strip model

Di Deng , Weiwen Zhao , Decheng Wan [*]

Computational Marine Hydrodynamics Lab (CMHL), State Key Laboratory of Ocean Engineering, School of Naval Architecture, Ocean and Civil Engineering, Shanghai Jiao Tong University, Shanghai, 200240, China

ARTICLE INFO

ABSTRACT

Numerical simulations on vortex-induced vibration (VIV) of a top tensioned flexible cylinder experiencing the uniform flow and the stepped flow conditions have been carried out by our in-house solver viv3D-FOAM-SJTU in this paper, which is developed by using the open source toolbox OpenFOAM and the three-dimensional strip model. Hydrodynamic forces in each three-dimensional fluid strip are calculated through the PIMPLE algorithm in the OpenFOAM adopting the Reynolds-averaged Navier-Stokes (RANS) method. The flexible cylinder is simplified as an Euler-Bernoulli bending beam, while structural vibrations are computed using the finite element method (FEM) in both the crossflow and the inline directions. The connection between three-dimensional fluid strips and the long flexible cylinder is realized through the interpolation of hydrodynamic forces and vibration displacements in each time step. Detailed comparisons on vibration Root Mean Square (RMS) amplitude, vibration frequency and vibration modes in both flow conditions among present simulation results, experimental results and published data are presented the validity of the viv3D-FOAM-SJTU solver. The fluid strip thickness dependence study shows that three-dimensional features of the wake field begins to appear at specific strip with dramatic vibration responses when the strip thickness reaches around 1/100 L (where L is the axial length of the flexible cylinder). The flow field of all fluid strips will be fully developed when the strip thickness reaches 3/100 L. Considering the cost of computational resources and the computational efficiency, the strip thickness around 1/50 L is recommend for future researches.

1. Introduction

Vortex-induced vibration (VIV) of a flexible riser has been extensively studied over the past decades around the world. In order to understand the characteristic of VIV, experimental and numerical methods are mainly adopted. Corresponding reviews can be referred to Sarpkaya (1979, 2004), Bearman, 1984, 2011, Williamson and Govardhan (2004), Gabbai and Benaroya (2005), Huang et al. (2009), Wu et al. (2012), Chen et al. (2016) and Wan and Duan (2017). As for model experiments, VIV of a flexible cylinder in steady flow conditions, such as uniform flow, sheared flow and stepped flow, are mainly investigated. Tognarelli et al. (2004) carried out experiments of a flexible riser in uniform and linearly sheared currents respectively to study the VIV features in different flow conditions. Trim et al. (2005) also carried out a series of experiments at the same flow conditions. VIV responses of a bare riser and a riser with various strake arrangements were mainly investigated.

Chaplin et al. (2005a, 2005b) conducted experiments of a vertical riser in stepped current with different top tension and the corresponding Reynolds number (*Re*) ranging from 3080 to 26600. Lie and Kaasen (2006) employed the modal analysis method that had been used by Chaplin et al. (2005b) to analyze the vibration features of a large-scale riser in linearly sheared flow. Song et al. (2016) investigated the distribution of drag force coefficients along the flexible riser span experiencing sheared flow through model tests. Song et al. (2011), Sanaati and Kato (2012) and Gedikli and Dahl (2017) carried out experiments of a flexible riser exposed to uniform flow too. Multi-modes vibration, effects of axial stiffness and pre-tension and mode excitation hysteresis features were studied.

In order to fully investigate the flow field around the flexible cylinder, the three-dimensional numerical model is used in some researches. Holmes et al. (2006) combined three-dimensional CFD solutions with structural models in simulating VIV of a straked riser. Huang et al.,

---

2007; Huang and Chen, 2007) presented a CFD approach for VIV prediction using the URANS method on the three-dimensional overset grid system. Numerical results on VIV of a flexible riser experiencing uniform flow and sheared flow were in good agreement with experimental results and previous publication data. Wang and Xiao (2016) adopted the Large Eddy Simulation (LES) method with the Arbitrary Lagrangian-Eulerian (ALE) scheme in simulating VIV response of a riser in uniform flow and sheared flow respectively using the ANSYS MFX multi-field solver.

Although the three-dimensional simulation method can reflect detailed flow characteristics, costs of the corresponding computational resources and the computational time are extremely huge especially when the cylinder aspect ratio (*L/D*, where *L* is the axial cylinder length and *D* is the cylinder diameter) is very large. Therefore, the traditional two-dimensional strip method used to predict the VIV response of risers was proposed by Willden and Graham (2001, 2004) to reduce both the computational resources and the computational time into an acceptable range. The strip method considered that the fluid flow was locally two-dimensional without spanwise correlation and simplified the three-dimensional fluid field into several two-dimensional strips uniformly distributed along the cylinder span. This method owns high computational efficiency and accuracy that has been verified through previous researches, such as Meneghini et al. (2004) and Yamamoto et al. (2004). Adopting the two-dimensional strip method, Duan et al. (2016a, 2018) developed the viv-FOAM-SJTU solver and carried out numerical simulations on VIV of a vertical riser exposed to the stepped current based on the experiments of Chaplin et al. (2005b) to verify the validity of the solver. Duan et al. (2016b, 2017) then studied effects of the cylinder aspect ratio (*L/D*) and the top tension (*T*) on VIV response. Fu et al. (2016, 2017), Fu and Wan (2017) mainly studied the effects of the cylinder mass ratio (*m* = m/m_ρ*, where *m* is the mass of the cylinder and *m_ρ* is the mass of the displaced water), the current profile and the cylinder top-end excitation on VIV response of a single cylinder using the viv-FOAM-SJTU solver. Fu et al. (2018) then further expanded the capacity of the solver in simulating VIV of a flexible cylinder experiencing oscillatory flow and validate its reliability compared with standard model experiments of Fu et al. (2013). However, the computational accuracy is hard to guarantee during high *Re* number flow condition or complicated fluid-structure interaction (FSI) problems.

Combining the advantages of considering the axial correlation effects from the three-dimensional method and the low computational resources and computational time cost from the traditional two-dimensional strip method, Bao et al. (2016) proposed the three-dimensional strip model (or named the generalized thick strip model) for VIV prediction of a long flexible cylinder using the direct numerical simulation (DNS) method. Then, Bao et al. (2019) conducted simulations on VIV of a single cylinder in uniform flow. Comparisons between experimental results and simulation results proved the validity of the thick strip method.

In this paper, the new viv3D-FOAM-SJTU solver is developed through modifying the previous viv-FOAM-SJTU solver by replacing the two-dimensional strip model with the three-dimensional strip model, and is applied to predict VIV response of a flexible cylinder exposed to the uniform flow and the stepped flow. This paper is organized as follows: The first section gives a brief introduction to the numerical methodology. The second section presents comparisons on VIV responses from present simulation, experiments and published data in the uniform flow condition, while the fluid strip thickness dependence study is also conducted in a detailed manner. The third section verifies the modified solver through comparisons on VIV features of a vertical flexible cylinder in stepped flow. And the final section concludes the paper.

2. Numerical method

2.1. Hydrodynamic governing equations

Hydrodynamic forces acted on the flexible cylinder are calculated from the viscous force and the pressure in each fluid strip, integrated over all boundary meshes on the cylinder surface. In order to solve the incompressible fluid flow locally, the Reynolds-averaged Navier-Stokes (RANS) method is employed. While the SST *k-ω* turbulence model, put forward by Menter (1993), is used to compute the Reynolds Stress with no wall functions used in present studies. Considering the cost of computational resources and the computational accuracy in the initial branch, the RANS method is more appropriate for the prediction of hydrodynamic forces than the Large Eddy Simulation (LES) method and the Direct Numerical Simulation (DNS) method in this paper. And the RANS method has been widely used in VIV simulations, such as Duan et al. (2017, 2018) and Fu et al. (2018). The continuity and the momentum equations for turbulent flow are written as Eq (1) and Eq (2):

$$\frac{\partial \overline{u}_i}{\partial x_i} = 0 \tag{1}$$

$$\frac{\partial}{\partial t}(\rho \overline{u}_i) + \frac{\partial}{\partial x_j}(\rho \overline{u}_i \overline{u}_j) = -\frac{\partial \overline{p}}{\partial x_i} + \frac{\partial}{\partial x_j}\left(2\mu \overline{S}_{ij} - \rho \overline{u'_j u'_i}\right) \tag{2}$$

where μ is the constant dynamic viscosity; ρ is the constant density; $\overline{S}_{ij} = \frac{1}{2}\left(\frac{\partial \overline{u}_i}{\partial x_j} + \frac{\partial \overline{u}_j}{\partial x_i}\right)$ is the mean rate of the strain tensor; $-\rho \overline{u'_j u'_i}$ is referred as the Reynolds stress τ_{ij} computed by $\tau_{ij} = -\rho \overline{u'_j u'_i} = 2\mu_t \overline{S}_{ij} - \frac{2}{3}\rho k \delta_{ij}$ where μ_t is the turbulent viscosity and $k = (1/2)\overline{u'_i u'_i}$ is the turbulent energy computing from the fluctuating velocity field; δ_{ij} is the Kronecke function.

The SST *k-ω* turbulence model put forward by Menter (1993) consists of turbulence kinetic energy *k* and turbulence dissipation rate *ω*. Transport equations of *k* and *ω* can be written as Eq (3) and Eq (4):

$$\frac{\partial(\rho k)}{\partial t} = \tau_{ij}\frac{\partial u_i}{\partial x_j} - \beta^* \rho \omega k + \frac{\partial}{\partial x_j}\left[(\mu + \sigma_k \mu_t)\frac{\partial k}{\partial x_j}\right] \tag{3}$$

$$\frac{\partial(\rho \omega)}{\partial t} = \frac{\gamma}{\mu_t}\tau_{ij}\frac{\partial u_i}{\partial x_j} - \beta \rho \omega^2 + \frac{\partial}{\partial x_j}\left[(\mu + \sigma_\omega \mu_t)\frac{\partial \omega}{\partial x_j}\right] + 2(1 - F_1)\frac{\rho \sigma_{\omega 2}}{\omega}\frac{\partial k}{\partial x_j}\frac{\partial \omega}{\partial x_j} \tag{4}$$

where $\mu_t = \frac{\rho a_1 k}{\max(a_1 \omega, \Omega F_2)}$ is the eddy viscosity; Ω is the vorticity; F_1 is the hydrodynamic function transiting *k-ω* model in the near wall to the *k-ε* model in outside the cylinder surface, which is defined as followed:

$$\phi = F_1 \phi_1 + (1 - F_1)\phi_2 \tag{5}$$

$$F_1 = \tanh\left(\text{arg}_1^4\right) \tag{6}$$

$$\text{arg}_1 = \min\left[\max\left(\frac{\sqrt{k}}{\beta^* \omega d}, \frac{500\nu}{d^2 \omega}, \frac{4\rho \sigma_{\omega 2} k}{CD_{k\omega} d^2}\right)\right] \tag{7}$$

$$CD_{k\omega} = \max\left(2\rho \sigma_{\omega 2}\frac{1}{\omega}\frac{\partial k}{\partial x_j}\frac{\partial \omega}{\partial x_j}, 10^{-20}\right) \tag{8}$$

$$F_2 = \tanh\left(\text{arg}_2^2\right) \tag{9}$$

$$\text{arg}_2 = \max\left(2\frac{\sqrt{k}}{\beta^* \omega d}, \frac{500\nu}{d^2 \omega}\right) \tag{10}$$

where $\beta^* = 0.09$; $\sigma_{k1}, \sigma_{\omega 1}, \beta_1, a_1, \gamma_1$ are the empirical coefficients in the *k-ω* model and $\sigma_{k2}, \sigma_{\omega 2}, \beta_2, \gamma_2$ are the empirical coefficients in the *k-ε* model.
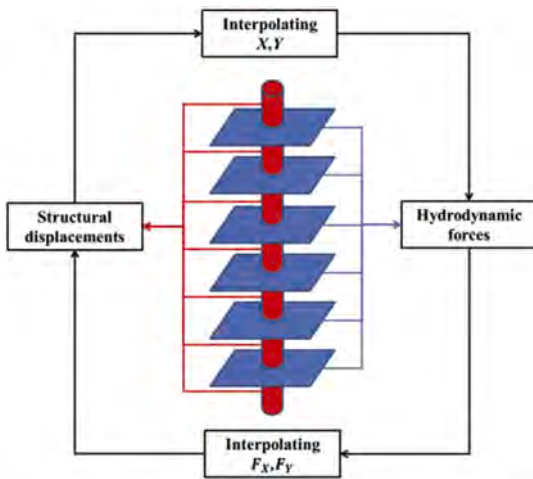
Fig. 1. Schematic diagram of the traditional strip theory.

Fig. 2. Computational thick strip model in viv3D-FOAM-SJTU solver.

2.2. Structural governing equations

Each thick fluid strip is independent and the connection between all strips is realized through the interpolation of the inline and the crossflow vibrations of the cylinder. The flexible cylinder is assumed to be an Euler-Bernoulli bending beam model with an axial pretension. The vibration of the model is solved through the FEM method and the structural governing equations in each structural element are written as Eq (11) and Eq (12).

$$m\ddot{x} + c\dot{x} + kx = f_x \tag{11}$$

$$m\ddot{y} + c\dot{y} + ky = f_y \tag{12}$$

where m, c, k are the mass, the damping and the stiffness of the structural element; f_x, f_y are the inline and the crossflow hydrodynamic forces

Table 1
Main parameters of model cylinder in uniform flow condition.

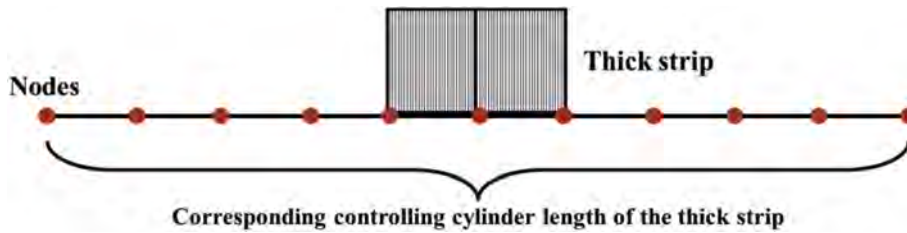|	Properties	Values	Unit
Length	L	9.63	m
Diameter	D	20	mm
Structural stiffness	EI	135.4	Nm^2
Top tension	T	817	N
Mass ratio	m*	2.23	–
Aspect ratio	L/D	481.5	–
Flow velocity	U	0.2	m/s

Fig. 3. Schematic diagram of one thick strip with its controlling cylinder length.

Fig. 4. Schematic diagram of the computational mesh update strategy.

3

(a) Computational model

(b) Computational domain of one strip

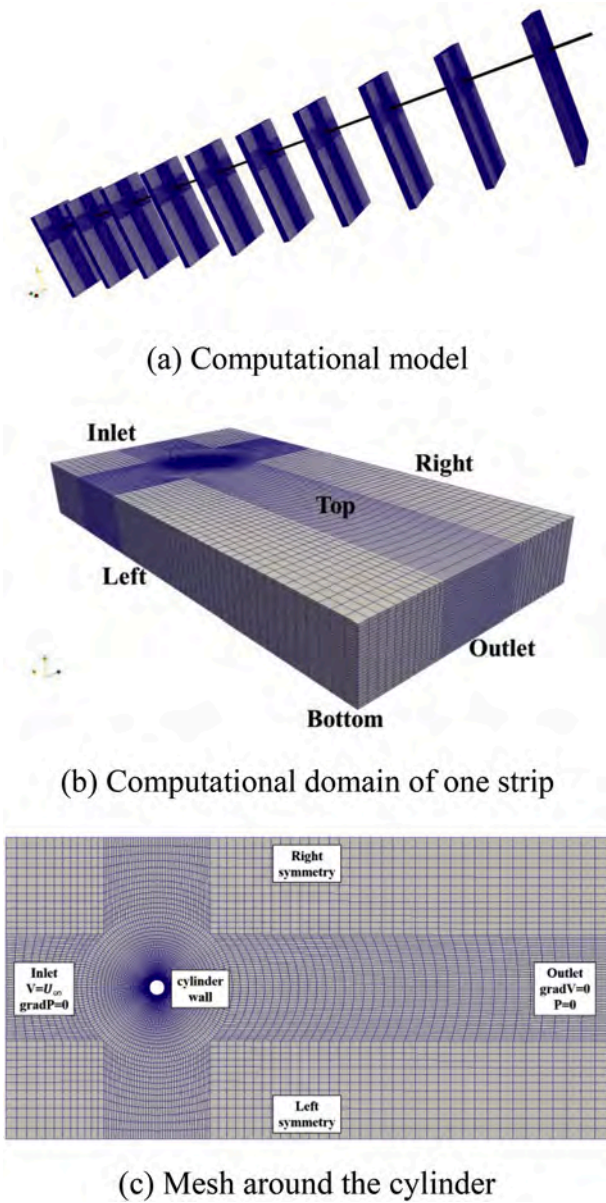(c) Mesh around the cylinder
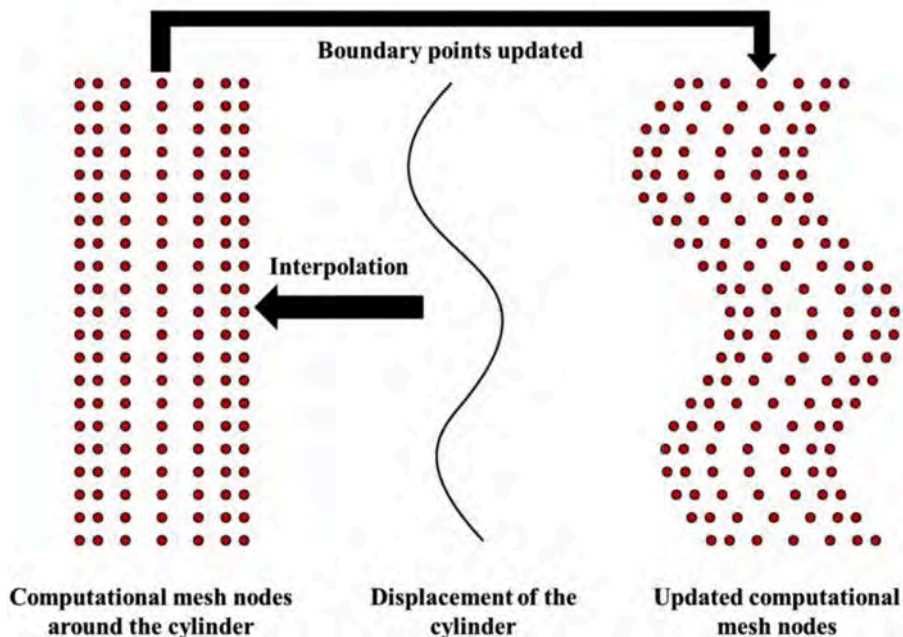
Fig. 5. Schematic diagram of the computational model in uniform flow.

respectively. Hence, the mass-spring-damping (MCK) equations of the whole system can be expressed as Eq (13) and Eq (14):

$$\mathbf{M}\{\ddot{\mathbf{X}}\} + \mathbf{C}\{\dot{\mathbf{X}}\} + \mathbf{K}\{\mathbf{X}\} = \{\mathbf{F_{HX}}\} \tag{13}$$

$$\mathbf{M}\{\ddot{\mathbf{Y}}\} + \mathbf{C}\{\dot{\mathbf{Y}}\} + \mathbf{K}\{\mathbf{Y}\} = \{\mathbf{F_{HY}}\} \tag{14}$$

where $\mathbf{M}$, $\mathbf{C}$, $\mathbf{K}$ are the mass, damping and stiffness matrixes of the system; $\{\mathbf{F_{HX}}\}$, $\{\mathbf{F_{HY}}\}$ are hydrodynamic force vectors in the inline and crossflow directions. Meanwhile, the Rayleigh damping is adopted to generate the damping matrix replacing the practical damping as shown in Eq (15) and Eq (16).

$$\mathbf{C} = a_0 \mathbf{M} + a_1 \mathbf{K} \tag{15}$$

$$\begin{bmatrix} a_0 \\ a_1 \end{bmatrix} = \frac{2\varsigma}{f_{n1} + f_{n2}} \begin{bmatrix} 2\pi f_{n1} f_{n2} \\ 1/(2\pi) \end{bmatrix} \tag{16}$$

where a_0 and a_1 are proportionality coefficient; ς is the damping ratio;

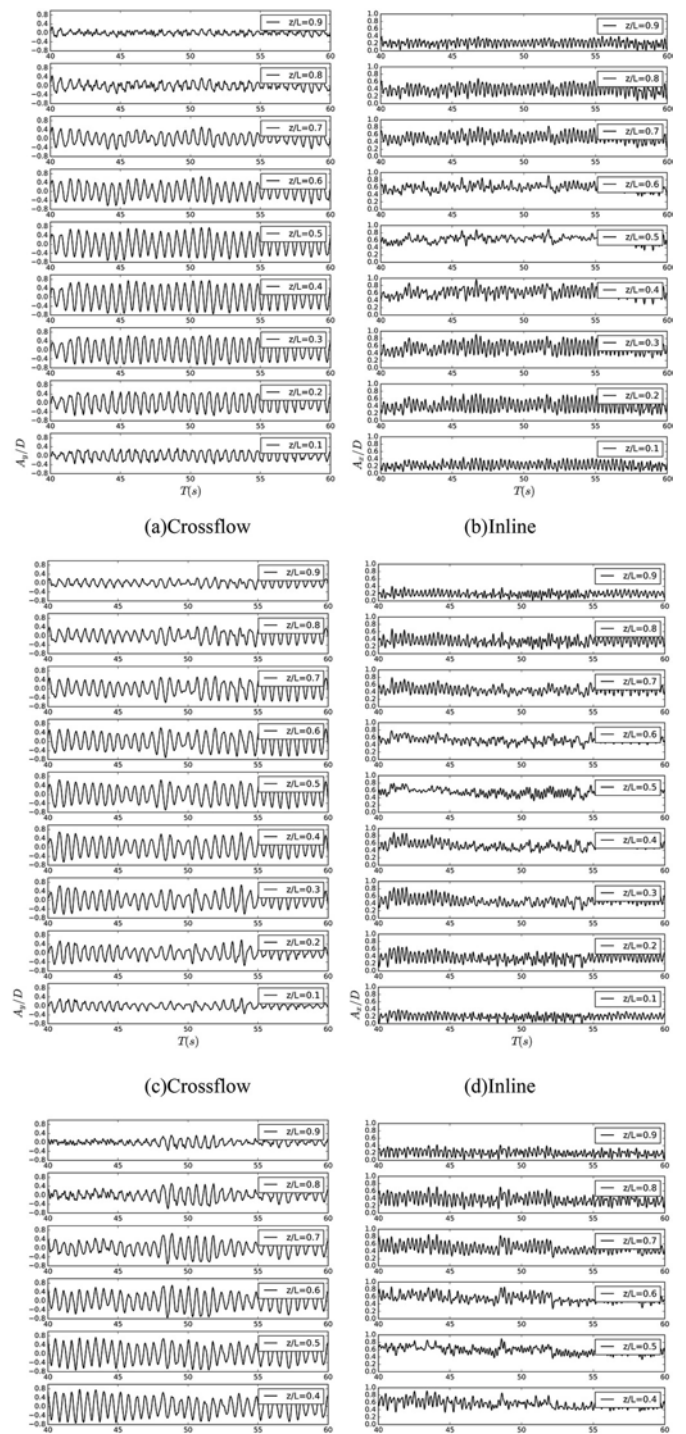(a)Crossflow (b)Inline

(c)Crossflow (d)Inline

Fig. 6. Time history vibration displacements along the cylinder span in both directions among three mesh resolutions: (a)coarse mesh; (b)coarse mesh; (c) middle mesh; (d)middle mesh; (e)fine mesh; (f)fine mesh.

f_{n1} and f_{n2} are the first and the second natural frequencies of the cylinder.

2.3. Three-dimensional strip model

The schematic diagram of the traditional two-dimensional strip theory is shown in Fig. 1. Due to the simplification on discretizing the three-dimensional fluid field around the cylinder into several two-dimensional fluid strips, the axial correlation and the three-dimensional characteristic of the shedding vortices are neglected
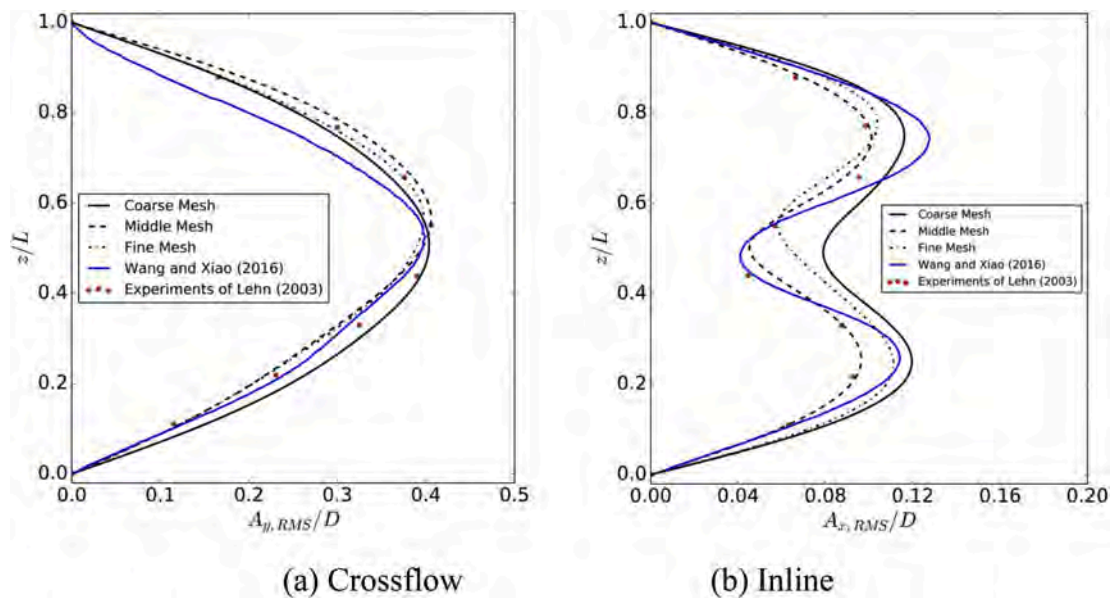
Fig. 7. Comparison of RMS amplitude along the cylinder span in both directions.
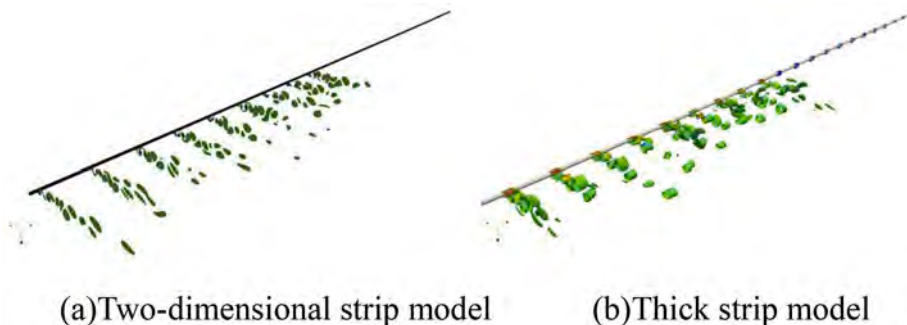

Fig. 8. Comparison on the vortex shedding phenomenon of a flexible cylinder using the traditional two-dimensional strip model and the thick strip model.

Table 2
Grid number of all computational conditions.

Case	Fluid strip thickness	Grid number
1	1/200 L	1.06 million
2	1/100 L	2.12 million
3	1/50 L	4.24 million
4	3/100 L	6.36 million
5	1/25 L	8.48 million
6	1/20 L	10.6 million

resulting in the underestimation of the hydrodynamic forces, especially at complicated flow fields. Then, the underestimated hydrodynamic forces will be transferred to the structural field and contribute to the inaccurate prediction of the vibration amplitudes compared to the experimental results, especially at high Re number experimental conditions.

To overcome the disadvantages of the traditional two-dimensional strip method, Bao et al.(2016) proposed the generalized thick strip model considering the spanwise correlation of the flow field locally. And the method had been validated in predicting VIV responses of a flexible cylinder by Bao et al.(2019).

In this paper, the thick strip model has been adopted to modify the previous viv-FOAM-SJTU solver and develop a new viv3D-FOAM-SJTU solver through replacing the two-dimensional fluid strips with locally three-dimensional thick fluid strips as shown in Fig. 2. In our thick strip

strategy, the thickness of the thick fluid strip is an integer multiple of the structural element length as shown in Fig. 3. Each thick strip owns its corresponding controlling axial length to conduct interpolation of the hydrodynamic forces and the vibration displacement between the thick fluid strip and the cylinder. Meanwhile, each thick strip contains the same number of computational boundaries at the cylinder surface for the calculation of hydrodynamic forces in both directions, which own the same length as one structural element. In each time step, hydrodynamic forces will be calculated in each thick strip and be transferred into uniformly distributed loads applied to the corresponding structural elements adopting the cubic spline interpolation method. Then, the inline and the crossflow vibrations of the cylinder are calculated using the FEM method through the Newmark-β algorithm, which has been explained by Tang (2002) and Clough (2003) in detail. Then, vibration displacements of all nodes in both directions can be obtained, which will be used to update the computational mesh of each thick fluid strip.

The computational mesh update strategy is shown in Fig. 4 where the boundary points are uniformly distributed on the cylinder surface in each thick strip. In order to guarantee the boundary mesh fitting the deformation shape of the corresponding cylinder part, the boundary points at the same axial position will be given the same vibration displacements in both x and y directions from the cylinder through the cubic spline interpolation method. The computational mesh will then be updated on the basis of the motions of the boundary points using the dynamic grid technique in the OpenFOAM at each time step.
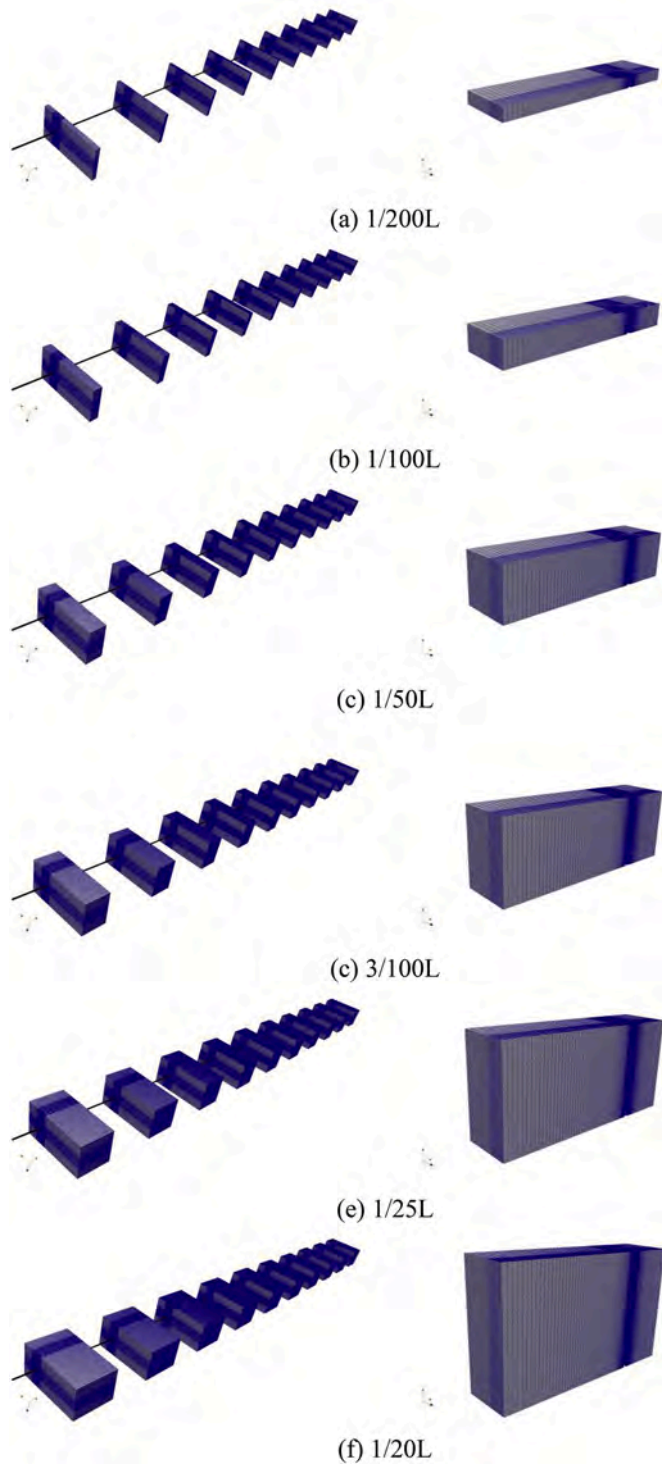
(a) 1/200L

(b) 1/100L

(c) 1/50L

(c) 3/100L

(e) 1/25L

(f) 1/20L

Fig. 9. Computational models and the corresponding mesh of the first thick fluid strip with different thickness.

3. VIV prediction in the uniform flow condition

3.1. Simulation model

Numerical simulations have been carried out based on the experiments of Lehn (2003) and the three-dimensional simulation of Wang and Xiao (2016). The model cylinder is located in the uniform flow with the cylinder aspect ratio $L/D = 481.5$ and the flow velocity $U = 0.2$ m/s. Main parameters of the model cylinder and the experimental setup are
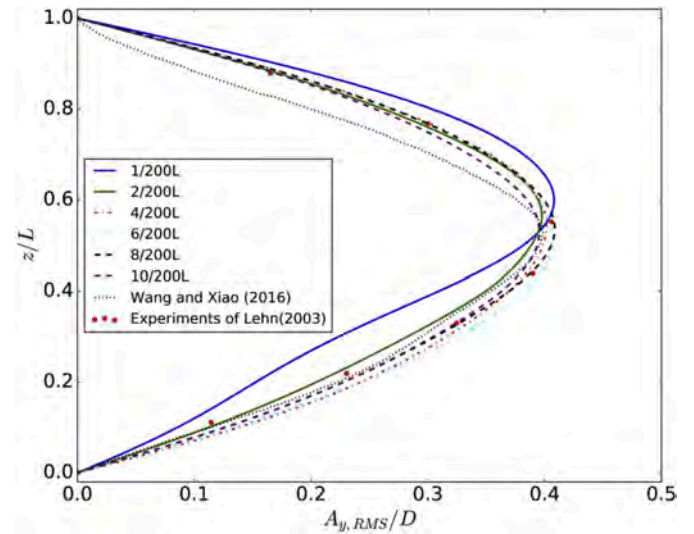

Fig. 10. Crossflow RMS amplitude comparisons between simulation results with different fluid strip thickness and the experiment result.

listed in Table 1.

All strips share the same computational mesh and boundary conditions. Detailed mesh around the cylinder in the thick fluid strip is shown in Fig. 5. The computational domain is 40D in the inline direction, 20D in the crossflow direction and 1/100 L in the vertical direction as shown in Fig. 5(a) where 10 thick fluid strips are uniformly located along the cylinder span. The computational mesh distribution is shown in Fig. 5 (c). In order to capture physical quantities in the boundary layer of the cylinder such as the velocity U and the pressure P, meshes near the cylinder surface are refined with no wall function used. Considering the choose of the SST k-ω turbulent model and the Re number, the y+ is set to be around 1.0 in all simulations to guarantee that meshes in the boundary layer of the flexible cylinder are fine enough to improve the computational accuracy of hydrodynamic forces. Corresponding boundary conditions are set as shown in Fig. 5(b) and (c): Velocity inlet condition is specified at the inlet boundary and pressure outlet condition is applied in the outlet boundary. Wall condition is specified at the cylinder surface boundary, while symmetry conditions are for the top, bottom, left and right boundaries. The flexible cylinder is discretized into 200 structural elements with 201 nodes in total. The time step is set as 0.001s to ensure the Courant Number (Co) lower than 5.0 during the implicit solution process, which guarantees the stability and the convergence rate in all simulations. Corresponding definition of the Courant Number is shown in Eq (17).

$$Co = \frac{U\Delta t}{\Delta x} \tag{17}$$

where U is the flow velocity; Δt is the time step; Δx is the size of the computational mesh near the cylinder surface. All simulations are computed in the high-performance computing (HPC) clusters adopting the parallel computing method to increase the computing efficiency, which decreases the computational time to around 20–30s for each time step. Correspondingly, one node with 28 cores are adopted for every 5.0 million cells.

3.2. Mesh convergence study

The computational mesh convergence study is carried out among three meshes with 2.12 million, 3.07 million and 4.13 million computational cells respectively to choose the appropriate mesh as the basic computational model. Time history of vibration displacements along the cylinder in both directions among three mesh resolutions are shown in Fig. 6. It can be found that locations near $z/L = 0.5$ present stable VIV
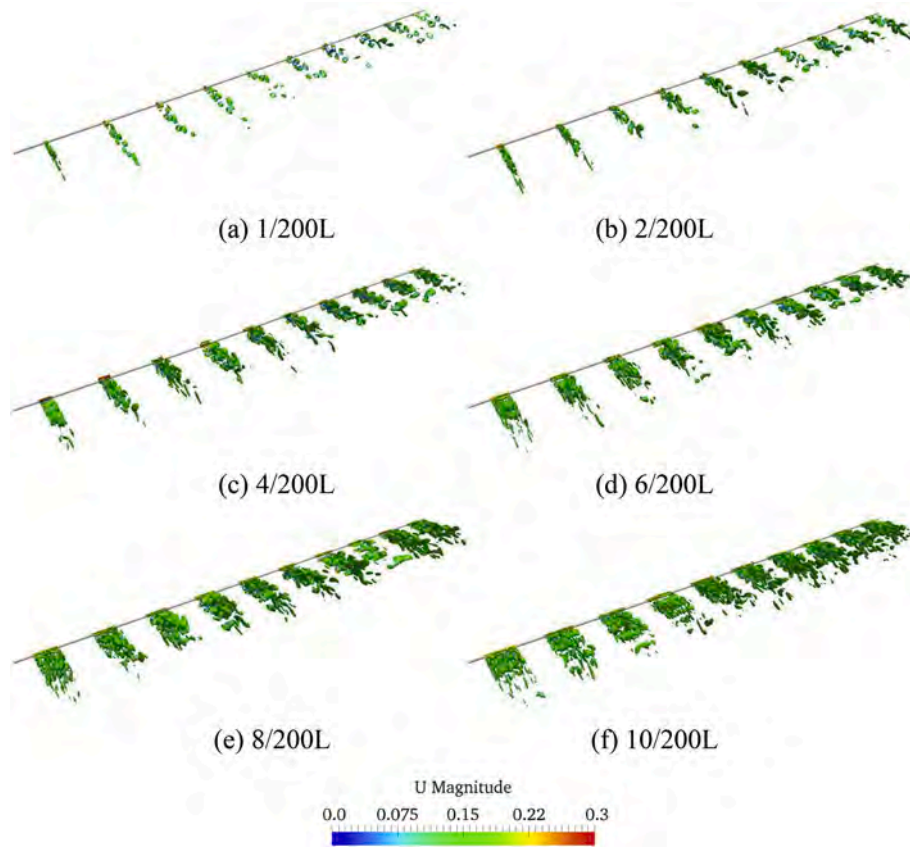
Fig. 11. Wake structures along the flexible cylinder span with different fluid strip thickness.

phenomenon with comparatively large vibration amplitude in the crossflow direction with the equilibrium position kept around 0 as shown in Fig. 6 (a), (c) (e). While similar vibration features can be observed near $z/L = 0.7$ and 0.3 in the inline direction, while the equilibrium position increases from around 0.2D to 0.6D and then decreases to 0.2D along the cylinder span.

Fig. 7 shows the vibration Root Mean Square (RMS) amplitude comparisons among experiments of Lehn (2003), simulation results of Wang and Xiao (2016) and present simulation results in both directions. The RMS amplitude can be obtained through Eq (18) and Eq (19):

$$A_{y,RMS}(z) = \sqrt{\sum_{t=t_s}^{t_e} \left[A_y(z,t)\right]^2} \tag{18}$$

$$A_{x,RMS}(z) = \sqrt{\sum_{t=t_s}^{t_e} \left[A_x(z,t) - \overline{A}_x(z)\right]^2} \tag{19}$$

where $A_{y,RMS}$ is the crossflow RMS amplitude; $A_{x,RMS}$ is the inline RMS amplitude; z is the axial location; t_s is the start time of the chosen interval; t_e is the end time of the chosen interval; $\overline{A}_x(z)$ is the equilibrium position along the cylinder in the inline direction during the chosen interval. The RMS amplitudes are in good agreement along the cylinder span as shown in Fig. 7(a). The maximum non-dimensional RMS vibration amplitude around 0.4D and the corresponding location around 0.55z/L are captured accurately. Although comparatively larger errors exist in the inline RMS amplitude comparisons as shown in Fig. 7(b). Both the middle mesh and the fine mesh capture the upper vibration RMS amplitude point around 0.092D at 0.22z/L, while only the middle mesh captures the nether vibration RMS amplitude point around 0.098D at 0.77z/L. Moreover, the RMS amplitude of the middle mesh agrees better with the model experiment than that from Wang and Xiao (2016),

especially in the inline direction. Based on the discussions above and taking the cost of computational resources into account, the middle mesh with an axial thickness of 1/100 L is chosen as the basic computational model for the following simulations.

3.3. Strip thickness effects on the VIV prediction

Fig. 8 shows comparison on the vortex shedding feature of a flexible cylinder in the stepped flow condition between the two-dimensional strip model and the thick strip model. It can be seen that vortices shed from the cylinder surface are out of phase along the cylinder span as well as the wake structure from Fig. 8(a). Meanwhile, three-dimensional wake fields can be observed in Fig. 8(b) and the wake structures will become more complicated around location where violent vibration appears.

Effects of the three-dimensional fluid strip thickness on VIV responses are mainly discussed in this section. 6 computational models with the fluid strip thickness varying from 1/200 L to 1/20 L are employed to study its influence on the VIV prediction in total. Corresponding grid number of each case is shown in Table 2, which increases from 1.06 million cells to 10.6 million cells. Three-dimensional fluid strip models and the corresponding mesh distribution of one strip with different thickness are shown in Fig. 8. When the strip thickness is around 1/200 L, the fluid strip only covers 5 percent of the cylinder length as shown in Fig. 9 (a), which is similar to the traditional two-dimensional strip model. When the strip thickness increases to 1/20 L, the fluid strips cover half the cylinder length that can be considered similar to the three-dimensional model as shown in Fig. 9 (f). All models are generated on the basis of the middle mesh above with the same grid distribution in the x-y plane and the same layers per structural element length in the axial direction.

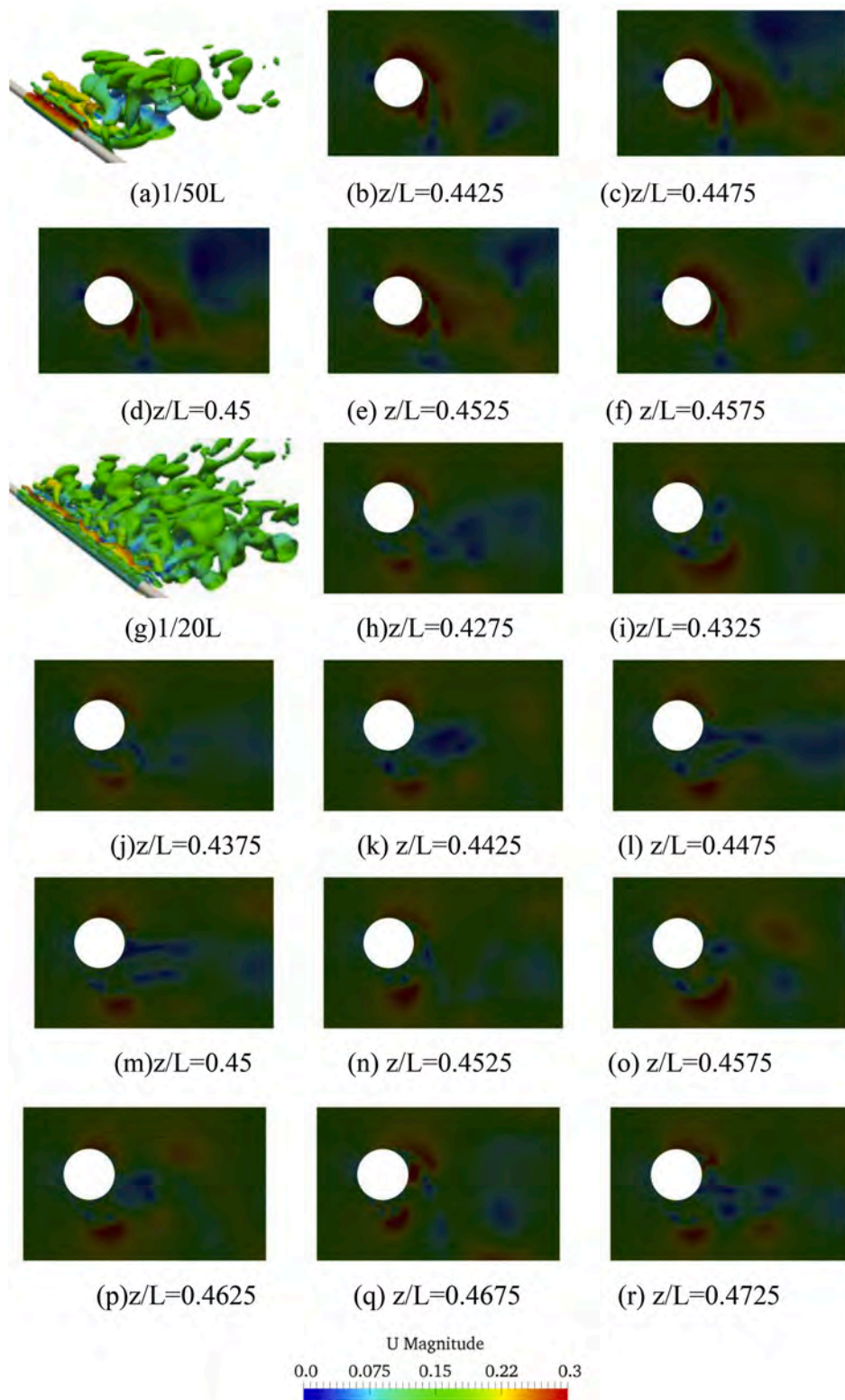Comparison on the crossflow RMS amplitude among present

Fig. 12. Instantaneous wake structures of the fifth fluid strip and the corresponding stream line graph with the strip thickness between 1/50 L and 1/20 L.

simulation results, the three-dimensional simulation of Wang and Xiao (2016) and the experiment of Lehn (2003) is shown in Fig. 10. Obvious errors can be found between the simulation with 1/200 L strip thickness and the result of Lehn (2003). The axial location corresponding to the maximum RMS amplitude is over predicted at around 0.6 L compared to around 0.55 L in the experiment. With the increase of the fluid strip thickness, both the maximum RMS amplitude and the corresponding

axial location are predicted more accurately. Simulation errors decrease rapidly between present simulations and Wang and Xiao (2016) when the fluid strip thickness is larger than 1/100 L, which also signifies that the three-dimensional characteristics of the wake structures beginning to be captured at 1/100 L fluid strip thickness. It can be concluded that the thin fluid strip thickness of the computational model may contribute to the inaccurate prediction of hydrodynamic forces, which then leads to
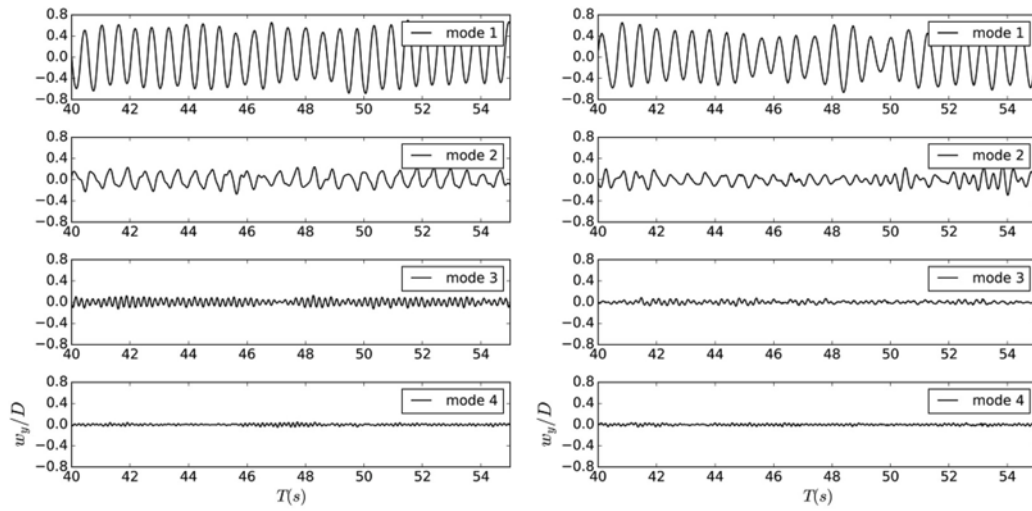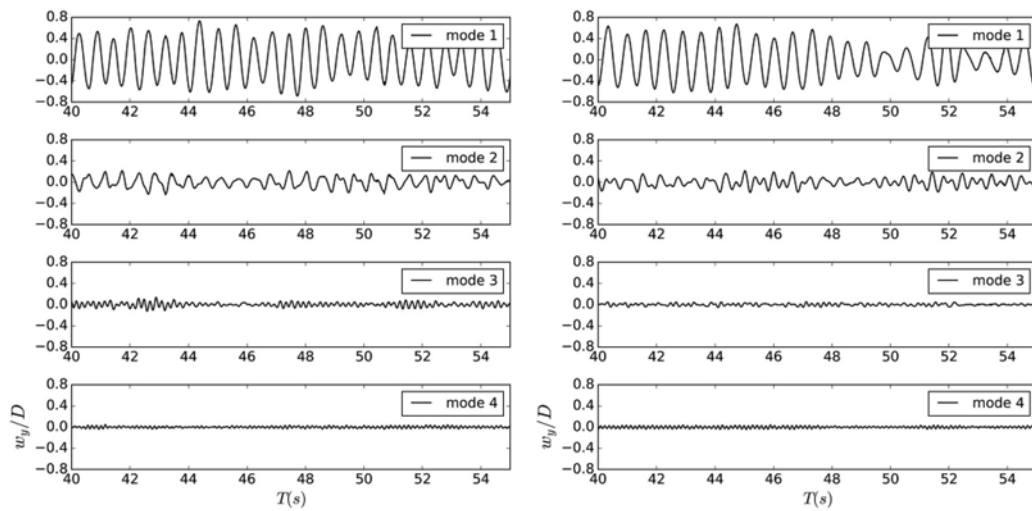
(a) 1/200L

(b) 1/100L
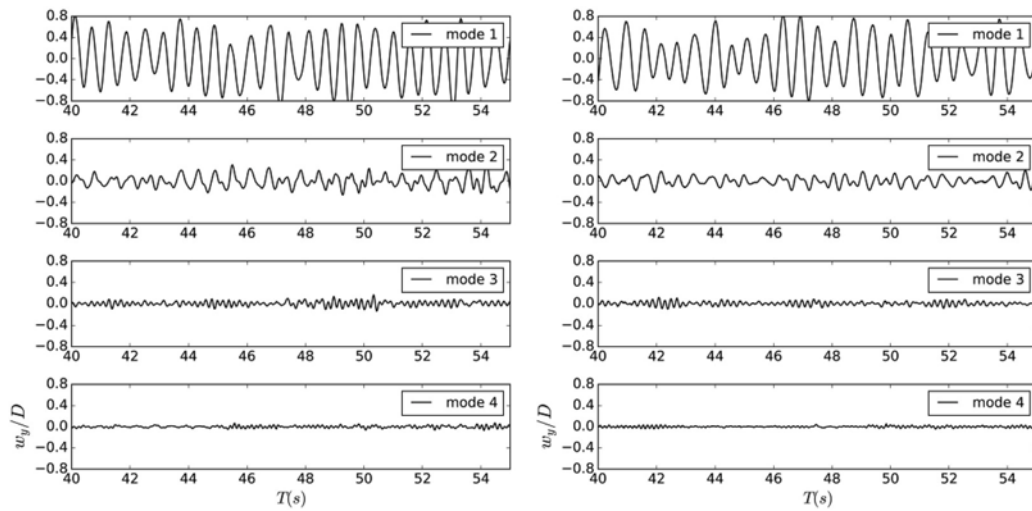
(c) 1/50L

(d) 3/100L

(e) 1/25L

(f) 1/20L

Fig. 13. Non-dimensional crossflow modal weights of the flexible cylinder with different strip thickness.
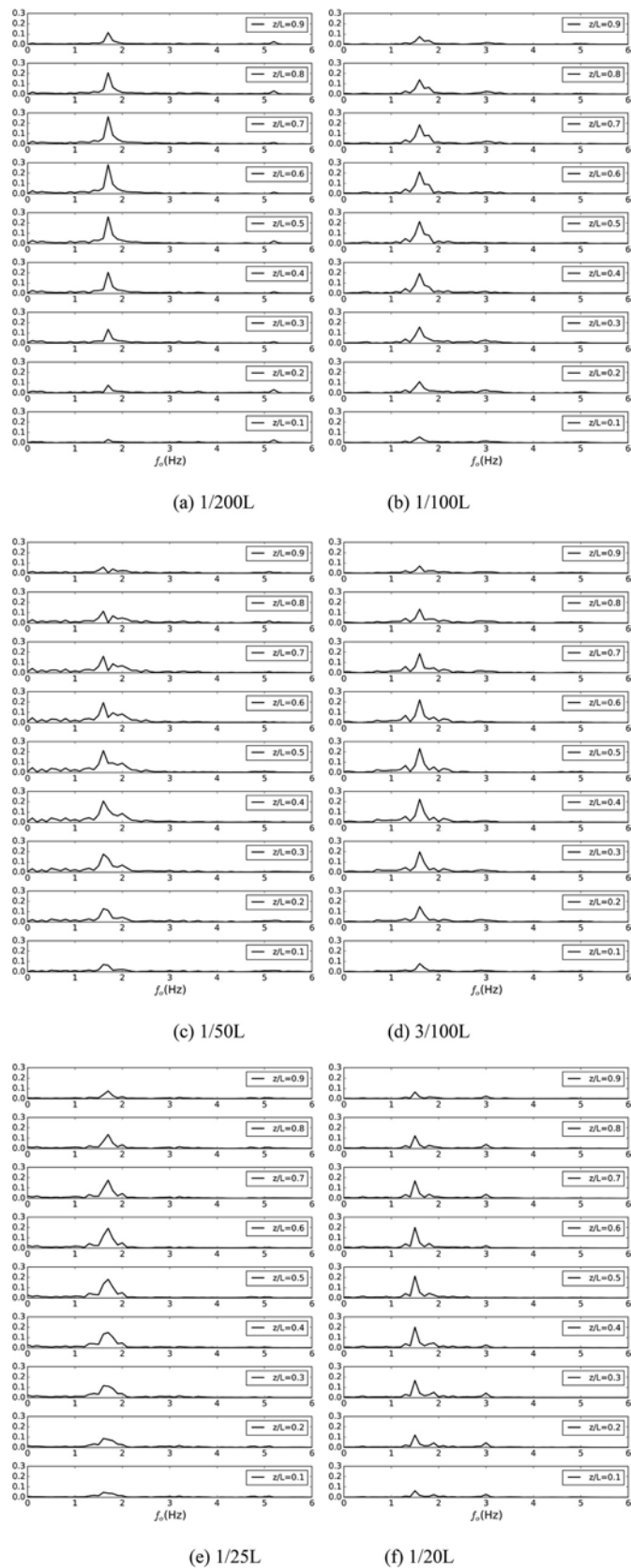
Fig. 14. Vibration frequency at nodes uniformly located along the cylinder span with different strip thickness.

Table 3
Main parameters of model cylinder in stepped flow condition.

	Properties	Values	Unit
Length	L	13.12	m
Diameter	D	0.028	mm
Structural stiffness	EI	29.88	Nm^2
Mass ratio	m*	3.0	–
Aspect ratio	L/D	469	–

Table 4
Simulation conditions in present study.

Case	Top tension (N)	Flow velocity (m/s)
7	405	0.16
8	407	0.21
9	457	0.31

the prediction errors in cylinder vibrations.

The dependence of the fluid strip thickness on VIV responses are dictated by the behavior of the wake structures in each thick strip, vibration frequency responses along the cylinder and the corresponding modal weights. Instantaneous spanwise wake structures of the flow for different strip thickness are shown in Fig. 11. These figures are generated through extracting three contour surfaces from the three-dimensional vorticity Q calculated using the OpenFOAM and then colored by the flow velocity U for clearer demonstration. It can be observed that the wake structure presents two-dimensional vortex shedding characteristics at thin strip thickness, which is very similar to the result calculated from the traditional two-dimensional strip model shown in Fig. 8(a). The shedding vortices hardly deform in the axial direction and keep the cylindrical shape, even though at the locations around z/L = 0.5 where drastic crossflow vibration happens and z/L = 0.25 and 0.75 where drastic inline vibration happens as shown in Fig. 11 (a). When the strip thickness increases to 1/100 L, three-dimensional vortex shedding phenomenon begins to appear especially at locations where drastic vibrations exist while the two-dimensional wake structures can also be observed at locations with weak VIV responses as shown in Fig. 11(b). However, the contour surface near the separation points along the cylinder span shows none wavy vortex generated near the cylinder surface due to the limitation of the strip thickness. It also means that the axial correlation length is larger than the strip thickness of 1/100 L. With the strip thickness increases to 1/50 L and the larger ones, fully three-dimensional wake structures cover almost all fluid strips as shown from Fig. 11(c)–(f). Meanwhile, the cylindrical type of three-dimensional vorticity becomes twisty resulting from the vibrations in both directions and the axial correlation effects. Wake structures present similar features among the strip thickness of 3/100 L, 1/25 L and 1/20 L, which can be considered that the strip thickness is large enough to cover the correlation length and the three dimensionality is fully developed.

Comparisons on the wake structures and the corresponding stream line graphs of the fifth strip between the strip thickness of 1/50 L and 1/20 L respectively are shown in Fig. 12. All two-dimensional stream line graphs are extracted uniformly along the selected thick strip and colored using the same parameter as the wake structure. It can be observed from Fig. 12(a)–(f) that a vortex has been shed from the cylinder surface and the distribution of the stream line around the vortex shows high similarity in the axial direction. Thus, none wavy type of vortex appears and the shedding vortex near the cylinder will show the cylindrical shape. However, the three-dimensional feature of the flow field will make the shedding vortex develop towards disordered and generate the discrete small vortices far from the cylinder surface as illustrated in Fig. 12(a), which leads to the axial variation of the latter vortices with blue color. An obvious wavy type of vortex can be observed in Fig. 12(g) when the strip thickness reaches 1/20 L. Corresponding stream line graphs from
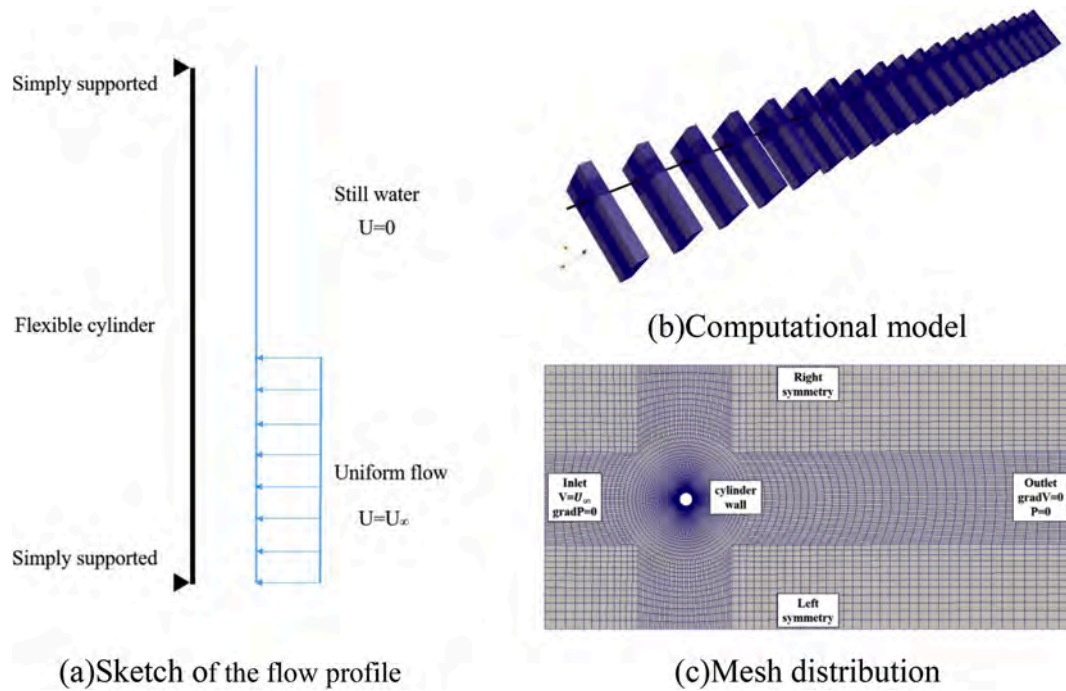
Fig. 15. The flow profile sketch along the water depth and the corresponding computational model of the flexible cylinder.

Table 5
Comparisons on the non-dimensional peak crossflow vibration amplitude.

	Case 7	Case 8	Case 9
Present simulations	0.772	0.502	0.791
Experiments	0.764	0.581	0.784
Norsk Hydro	0.182	–	0.520
USP	0.412	0.520	0.561
DeepFlow	0.696	–	0.703
VIVIC	0.899	–	0.493

Fig.12(h)–(r) show remarkable variation on the velocity distribution at both the vicinity of the cylinder surface and the distal end of the flow field along the axial direction. The magnitude of the contour region with red color under the cylinder fluctuates along the strip span synchronized with the axial deformation of the shedding wavy vortex shown in Fig. 12 (g).

In order to analyze the modal vibration features of the flexible cylinder, the modal decomposition method is adopted, which has been verified by Chaplin et al. (2005a) and Fu et al. (2018). The vibration displacements of the cylinder in both directions can be divided into a series of modal shapes as followed:

$$\phi_n(z) = \sin\left(\frac{n\pi}{L}z\right) \qquad (20)$$

$$x(z,t) = \sum_{n=1}^{N} u_n(t) \cdot \phi_n(z) \qquad (21)$$

$$y(z,t) = \sum_{n=1}^{N} v_n(t) \cdot \phi_n(z) \qquad (22)$$

where z is the axial location of the cylinder nodes; L is the cylinder length; n = 1, 2, 3 and etc; $x(z,t)$ is the inline displacement; $y(z,t)$ is the crossflow displacement; $u_n(t)$ is the time-dependent modal weight in the inline direction; $v_n(t)$ is the time-dependent modal weight in the crossflow direction and N is the mode number. In each time step, the instantaneous modal weights of each mode can be calculated and the dominant vibration mode of the cylinder can be judged through the modal weight comparison during the analyzed interval.

Non-dimensional crossflow modal weights of the flexible cylinder for the first four orders with different strip thickness are shown in Fig. 13. It can be concluded that the dominant vibration mode keeps the same first mode in all simulation models in the crossflow direction as the experiment. Although the non-dimensional modal weight of the second vibration mode reaches around 0.2, it is still covered by the first mode resulting in the hidden of the second mode. Meanwhile, non-dimensional modal weights of the third mode and the fourth mode are extremely small compared to the first mode that contribute to the single mode vibration phenomenon, which agree with the vibration frequency responses in Fig. 14.

The Fast Fourier Transform Algorithm (FFT) is adopted to calculate the vibration frequency responses of nodes uniformly located along the cylinder span as shown in Fig. 14. It can be found that only one frequency peak corresponding to around 1.6 Hz appears in almost all nodes. The peak amplitude of the dominant vibration frequency increases and then decreases along the cylinder presenting similar variation as the vibration RMS amplitude, which contribute to the appearance of the first dominant vibration mode in Fig. 13. The dominant vibration frequency shows a narrow bandwidth when the strip thickness is 1/200 L. With the increase of the strip thickness, the bandwidth increases too and more peaks with comparative small values appear around the dominant vibration frequency that may result from the three-dimensional feature of the flow field especially at large strip thickness model.

4. VIV prediction in the stepped flow condition

4.1. Simulation model

In order to verify the viv3D-FOAM-SJTU solver furtherly, numerical simulations based on the experiments of Chaplin et al. (2005a) and Huera Huarte (2006) are conducted. Comparisons have been conducted among the present simulations, the experimental results and the published data in a detailed manner. The lower 45% part of the vertical cylinder model is located in the uniform flow as shown in Fig. 5(a), while the upper part is in still water that generates the stepped flow condition.
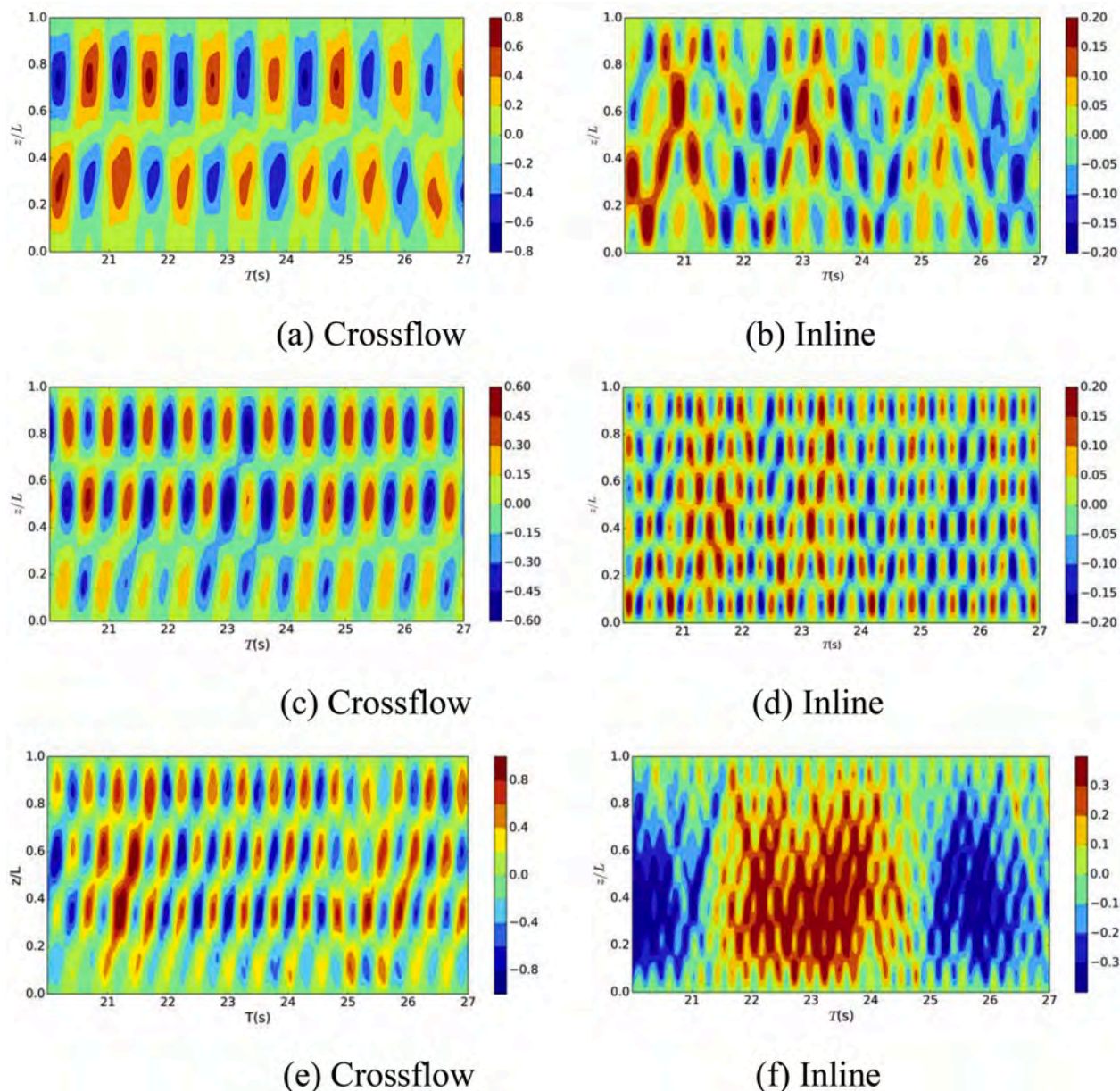
Fig. 16. Spatiotemporal Vibration displacement contours in both the crossflow and the inline directions among three computational cases. (Case 7: a, b; Case 8: c, d; Case 9: e, f).

Three groups of top tension T and flow velocities U are chosen. Main parameters of the cylinder model and the corresponding simulation conditions are shown in Table .3 and Table .4.

The computational model and the corresponding mesh distribution based on the middle mesh case in the previous part are shown in Fig. 15. The Euler-Bernoulli beam hypothesis is also adopted with the cylinder model been discrete into 200 elements during the calculation of structural vibrations through the FEM method. Considering the computational cost and the computational efficiency, the thickness of each fluid strip is set as 1/100 L that the three-dimensional vortex shedding phenomenon will appear at locations where drastic axial deformation happens. Through researches of Willden and Graham (2001, 2004), they found that a minimum of three fluid strips were required per vibration mode for the correct capture on the axial variation of the phasing of the hydrodynamic forces with respect to the cylinder vibration. Therefore, 20 thick fluid strips, containing 40 structural elements, are used and uniformly located along the cylinder span, which are sufficient to capture the maximum fourth mode in the crossflow direction and seventh

mode in the inline direction. Thus, the lower 9 strips are set the same flow velocity as the experiments and the flow velocity in the rest strip are set zero to simulate the still water condition. The computational model is shown in Fig. 15(b), while boundary conditions of each thick fluid strip are the same as that shown in Fig. 5(b). There are 6.16 million cells in total and the mesh distribution in the x-y plane is shown in Fig. 15(c), which is similar to that shown in Fig. 5(c).

4.2. Comparisons on VIV responses

The experimental results from Chaplin et al. (2005a), the blind prediction results from Chaplin et al. (2005a, different simulation codes used in their researches) and the present simulation results are compared in a detailed manner in this part as shown in Table .5. The Norsk Hydro, the USP (University of São Paulo), the DeepFlow (Institut Francais du Pétrole) and the VIVIC developed by Graham and Willden (2004, at Imperial College, London) are simulation codes developed by former researchers using Computational Fluid Dynamic techniques
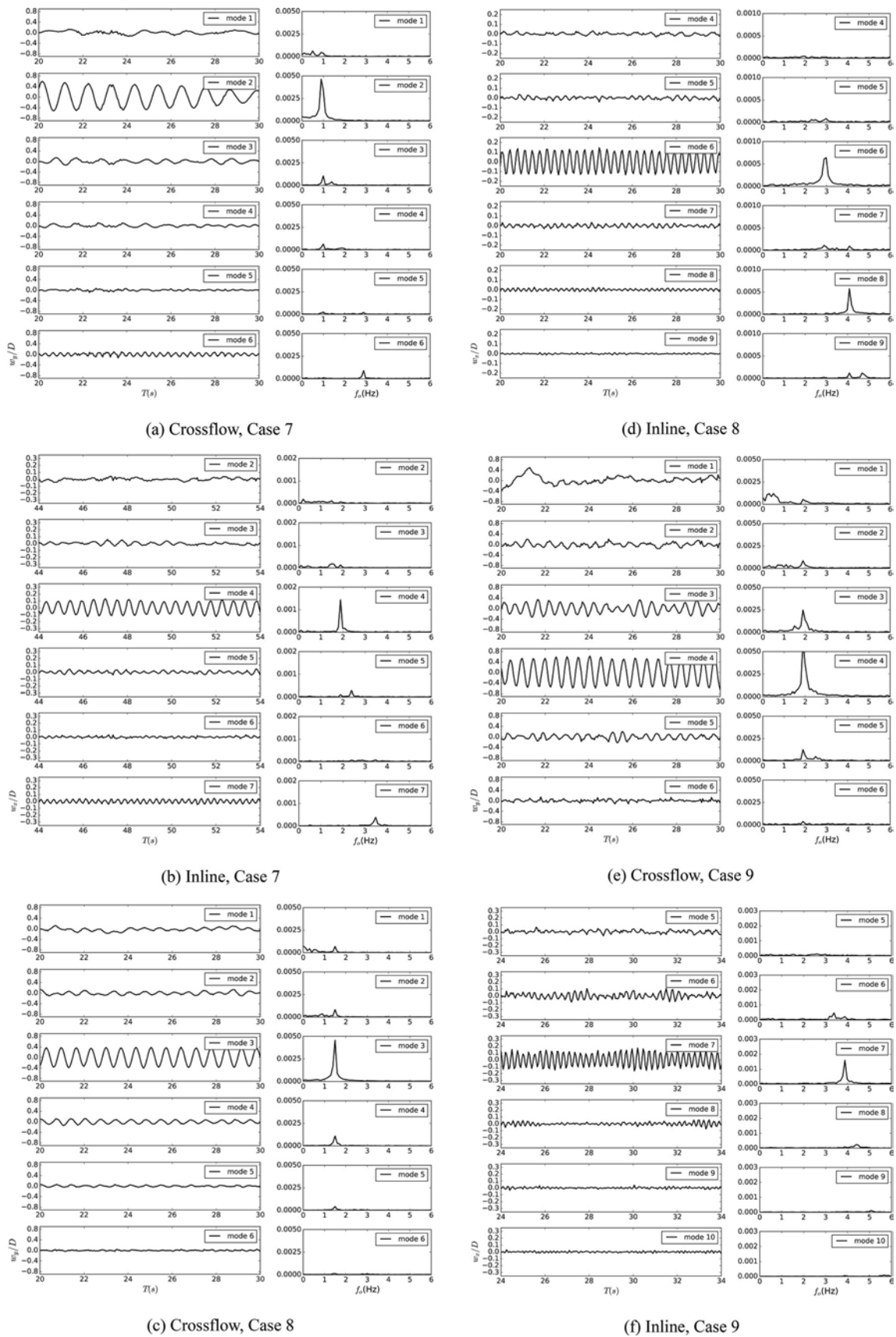
(a) Crossflow, Case 7

(b) Inline, Case 7

(c) Crossflow, Case 8

(d) Inline, Case 8

(e) Crossflow, Case 9

(f) Inline, Case 9

Fig. 17. Modal decomposition results in both the crossflow and the inline directions among three computational cases.

Table 6
Comparisons on the dominant vibration mode in the crossflow direction.

	Present simulations		Experiment	
	Crossflow	Inline	Crossflow	Inline
Case 7	2	4	2	4
Case 8	3	6	3	6
Case 9	4	7	4	7

Table 7
Comparisons on the dominant vibration frequency in the crossflow direction.

	Present simulations	Experiment	Computational error
Case 7	0.902 Hz	0.995 Hz	9.35%
Case 8	1.5 Hz	1.345 Hz	11.5%
Case 9	1.9 Hz	1.966 Hz	3.36%

combined with two-dimensional strip method. It can be found that the predicted results on the maximum non-dimensional crossflow vibration amplitude are 0.772 and 0.791 in case 7 and case 9 using the

viv3D-FOAM-SJTU solver, which are closer to the experimental results of 0.764 and 0.784 than the simulation results from almost other simulation codes. Although the computational error reaches around 13.6% in case 8 that is larger than the result from the USP, the validity of the solver can still be verified through comparisons above.

Spatiotemporal vibration displacement contours in both the crossflow and the inline directions among three computational cases are shown in Fig. 16. The crossflow vibration shows the second mode shape in case 7, the third mode shape in case 8 and the fourth mode shape in case 9, while the typical standing wave phenomenon is observed from Fig. 16 (a), (c) and (e). It can be found that the non-dimensional crossflow vibration amplitude decreases from around 0.8 to 0.5 and then increases with both the top tension and the flow velocity increase. Meanwhile, the corresponding inline mode shapes are the fourth mode, the sixth mode and the seventh mode respectively. The obvious travelling wave phenomenon can be observed during the time span. And the non-dimensional inline vibration amplitude behaves similar variation as that in the crossflow direction, which decreases from around 0.2 to 0.15 and then increases to 0.25. Comparatively, the maximum non-dimensional inline vibration amplitudes are 0.211, 0.101 and 0.301
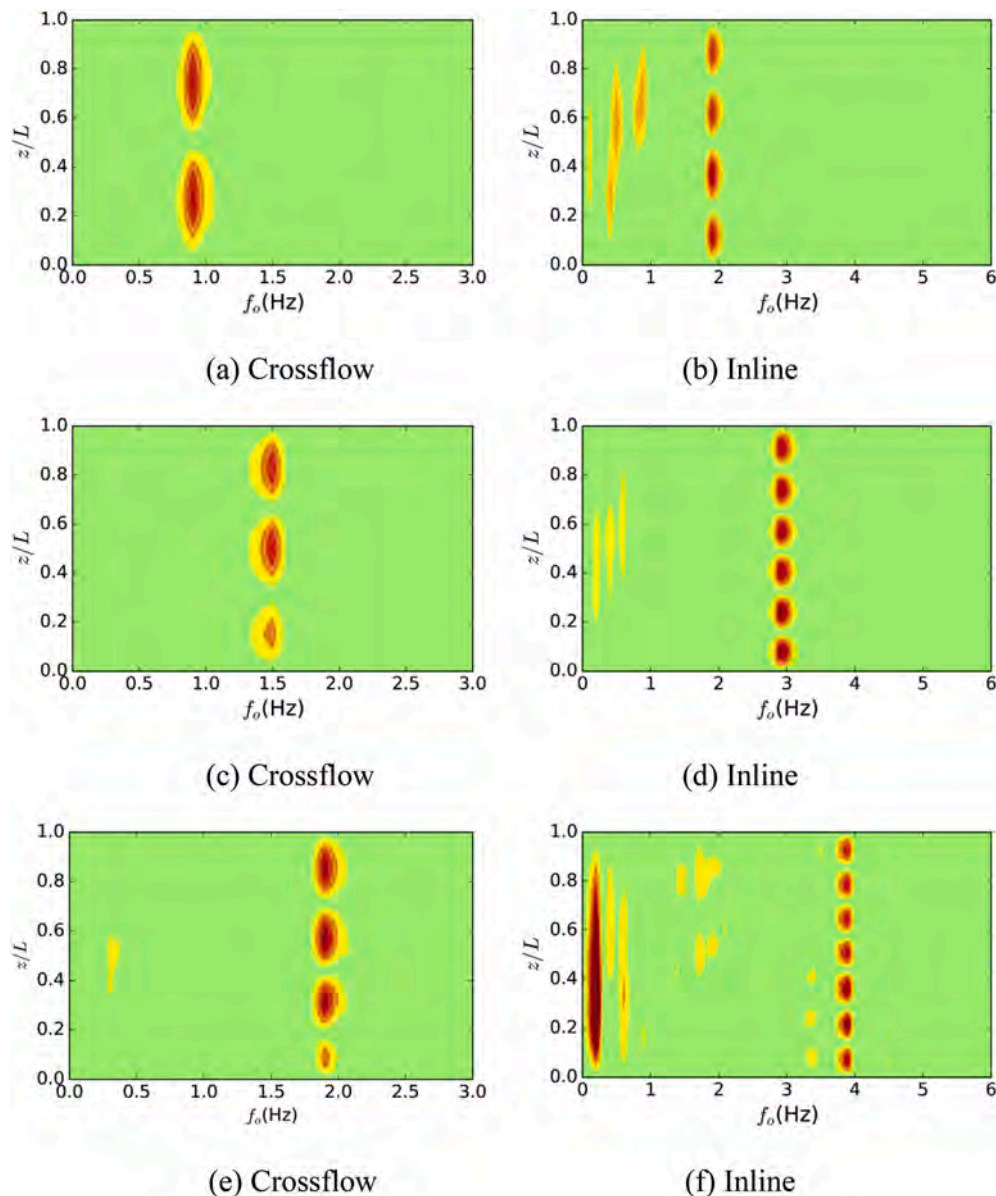

Fig. 18. Crossflow vibration frequency contours along the cylinder span among three computational conditions, (Case 7: a, b; Case 8: c, d; Case 9: e, f).
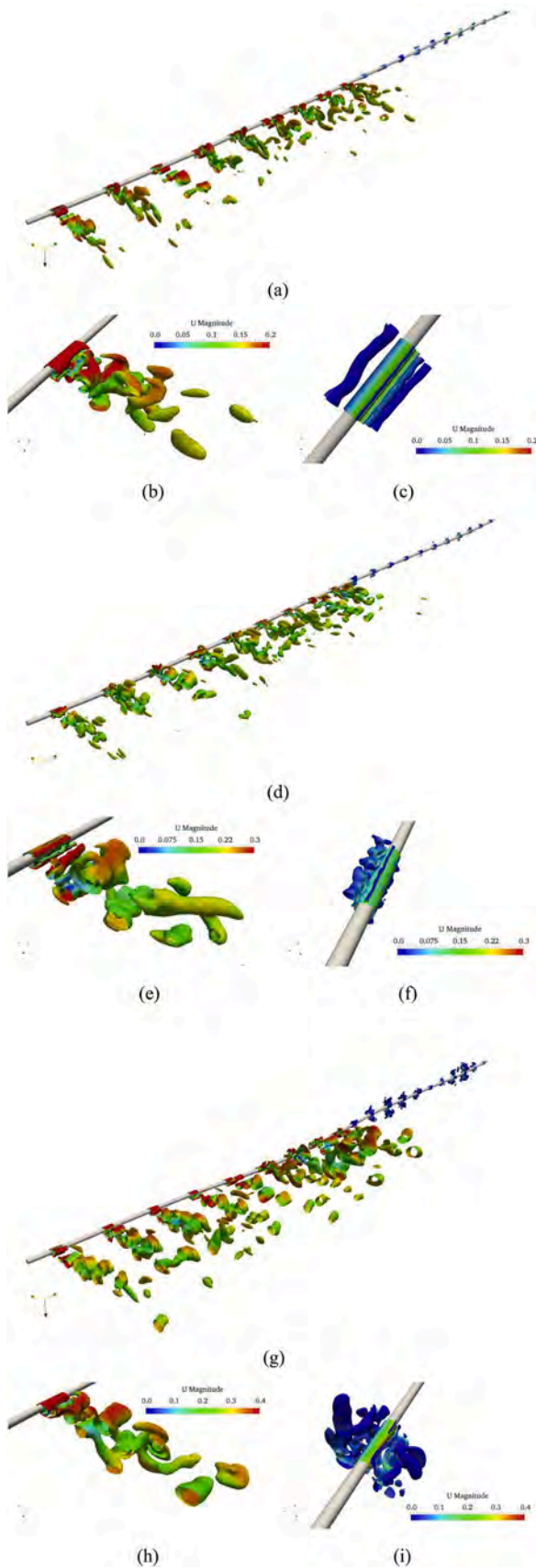
Fig. 19. Instantaneous wake structures along the cylinder span and specific thick fluid strips among three computational conditions, (Case 7: a, b, c; Case 8: d, e, f; Case 9: g, h, i).

respectively in the experiments that is similar to the variation shown in the inline spatiotemporal contours from Fig. 16(b), (d) and (f).

The modal decomposition results and the corresponding modal vibration frequency in both directions among three computational conditions are shown in Fig. 17. Through comparisons on the temporal modal weights among different vibration modes, it can be concluded that both the crossflow and the inline vibrations present the single dominant vibration mode phenomenon, corresponding vibration modes are the second mode, the third mode and the fourth mode in the crossflow direction and the fourth mode, the sixth mode and the seventh mode in the inline direction. Modal vibration features show high similarity compared with the spatiotemporal contours in Fig. 16. With the increase of the cylinder top tension and the flow velocity, effects of higher vibration modes are enhanced obviously, especially in the inline direction as shown in Fig. 17(e) where values of the third modal weight is close to that of the dominant fourth mode. However, the controlling effects of the dominant vibration mode cover the effects of other vibration modes contributing to the behavior of the single mode vibration phenomenon. Comparisons on the dominant vibration modes between experiments of Chaplin et al. (2005a) and present simulations are shown in Table 6 where good agreements are obtained in all computational conditions. The dominant inline vibration mode is twice of the dominant crossflow vibration mode in case 7 and case 8, while it decreases to 1.75 times of the dominant crossflow vibration mode in case 9.

As for the corresponding dominant vibration frequency features, it increases from around 1.0 Hz to around 2.0 Hz with an interval of around 0.5 Hz in the crossflow direction along with the increase of the top tension and the flow velocity. Meanwhile, the dominant inline vibration frequency increases from around 2 Hz to around 4 Hz with an interval of 1 Hz, which is twice of the dominant crossflow vibration frequency in all computational conditions.

Comparisons on the dominant vibration frequencies between the experiments and the present simulations among three computational conditions in the crossflow direction are shown in Table .7. The predicted dominant vibration frequencies are 0.902 Hz, 1.5 Hz and 1.9 Hz respectively from the present simulations, while the experimental results present 0.995 Hz, 1.345 Hz and 1.966 Hz respectively among these cases. The maximum computational error reaches 11.5% in case 8 and the minimum error only reaches 3.36% in case 9. Corresponding vibration frequency contours along the cylinder span in both directions are shown in Fig. 18. It can be observed from Fig. 18(a), (c) and (e) that the vibration frequency regions are mainly located around the dominant vibration frequency in the crossflow direction. The variation of the frequency region along the cylinder span presents the same modes as shown in the vibration displacement contours in Fig. 16. Meanwhile, similar phenomenon can be observed from Fig. 18(b), (d) and (f) in the inline direction. The only difference is that lower vibration frequency components paly non-negligible effects on VIV responses in the inline direction contributing to the obvious first mode inline deformation of the cylinder especially at high *Re* condition as shown in Fig. 18(f) where the lower vibration frequency around 0.2 Hz presents the same magnitude of spectral density as the dominant vibration frequency. While the corresponding dominant vibration frequencies are 1.899 Hz, 2.9 Hz and 3.897 Hz respectively in the inline direction that are twice of the crossflow vibration frequencies.

The instantaneous wake structures of the cylinder with different top tensions and flow velocities are shown in Fig. 19 respectively. It can be found that the obvious vortex shedding phenomenon can be observed on the lower part of the cylinder. The wavy type of vortices near the separation points also appears especially at location where dramatic vibration occurs. However, the wake structures are not fully developed at all fluid strips due to the combined effects of the strip thickness and the corresponding vibration amplitude, such as the third strip in Fig. 19(a) and the fifth strip in Fig. 19(g). Contributing to the effect of the stepped flow condition, the generated vortices in the lower nine strips are shedding in the inline direction, while vortices in the upper eleven strips

are shed mainly in the crossflow direction with comparative smaller magnitude as comparisons among Fig. 19(b), (e), (h) and Fig. 19(c), (f), (i). It can be concluded that the vortex shedding direction in the lower strips mainly controlled by the incoming flow, while the vortex shedding direction in the upper strips is determined by the vibration strength of the cylinder in both directions. With the increase of the top tension and the flow velocity, the vortices strength and the three-dimensional vortex shedding characteristic of the upper strips become more obvious, which develops from the cylindrical vortices to the discrete small vortices as shown from Fig. 19(c), (f) and (i).

5. Conclusions

The new viv3D-FOAM-SJTU solver is developed by using three-dimensional strip model (or named the thick strip model) to modify the previous viv-FOAM-SJTU solver with considering the axial correlation of the flow field in each fluid strip, and adopted to predict VIV responses of flexible cylinders. The validity of the viv3D-FOAM-SJTU solver has been verified through a series of comparisons among experimental results, published data and present simulation results. Two benchmark experiments from Lehn (2003) in the uniform flow condition and Chaplin et al. (2005a) in the stepped flow condition are mainly chosen and compared in detail. VIV responses of the vibration RMS amplitude, the dominant vibration mode and the dominant vibration frequency from present simulations show good agreement with the experiments. The fluid strip thickness dependence study is conducted in the uniform flow condition. With the increase of the strip thickness, the three-dimensional vortex shedding phenomenon becomes more obvious and the wavy type of vortices can be observed near the separation points. When the strip thickness is lower than $1/200\,L$, the vortex shedding phenomenon presents high similarity to that calculated from the two-dimensional strip model. The flow fields will be fully developed when the corresponding strip thickness is larger than $3/100\,L$. Both the cylindrical type of vortices and the discrete vortices can be observed in the wake structures when the strip thickness is around $1/100\,L$ combing the vortex shedding features of both the two-dimensional strip model and the three-dimensional model.

Declaration of competing interest

Our research interest is mainly on Computational Marine Hydrodynamics, Ship Flows, Sea-keeping, Maneuverability, Simulation Based Design for Offshore and Polar Structures, Renewable Energy in Deep Sea, numerical marine basin, nonlinear wave theory, wave loads on structures, numerical analysis of riser vortex-induced vibration (VIV) and platform vortex-induced motion (VIM), fluid-structure interaction, offshore wind turbine and other offshore renewable resources, as well as high performance computation on complex ship and ocean engineering flows, etc.

CRediT authorship contribution statement

Di Deng: Conceptualization, Methodology, Software, Data curation, Visualization, Investigation, Validation, Writing - original draft. **Weiwen Zhao:** Visualization, Investigation, Validation. **Decheng Wan:** Supervision, Investigation, Validation, Writing - review & editing.

Acknowledgments

References

Bao, Y., Palacios, R., Graham, M., et al., 2016. Generalized thick strip modelling for vortex-induced vibration of long flexible cylinders[J]. J. Comput. Phys. 321 (800), 1079–1097.

Bao, Y., Zhu, H.B., Huan, P., et al., 2019. Numerical prediction of vortex-induced vibration of flexible riser with thick strip method[J]. J. Fluid Struct. 89, 166–173.

Bearman, P.W., 1984. Vortex shedding from oscillating bluff body[J]. Annu. Rev. Fluid Mech. 16, 195–222.

Bearman, P.W., 2011. Circular cylinder wakes and vortex-induced vibrations[J]. J. Fluid Struct. 27, 648–658.

Chaplin, J.R., Bearman, P.W., Cheng, Y., et al., 2005a. Blind predictions of laboratory measurements of vortex-induced vibrations of a tension riser. J. Fluid Struct. 21, 25–40, 1 SPEC. ISS.

Chaplin, J.R., Bearman, P.W., Huera Huarte, F.J., et al., 2005b. Laboratory measurements of vortex-induced vibrations of a vertical tension riser in a stepped current[J]. J. Fluid Struct. 21, 3–24, 1 SPEC. ISS.

Chen, W.M., Fu, Y.Q., Guo, S.X., et al., 2016. Fluid-solid coupling and hydrodynamic response of vortex-induced vibration of slender ocean cylinders[J]. Adv. Mech. 38, 604, 05.

Clough, R.W., 2003. Penzien J. Dynamics of structures. In: Computers & Structures, third ed. Inc., Berkeley.

Duan, M.Y., Wan, D.C., Xue, H.X., 2016a. Prediction of response for vortex-induced vibrations of a flexible riser pipe by using multi-strip method[C]. In: Proceedings of the Twenty-Sixth (2016) International Ocean and Polar Engineering Conference Rhodes, pp. 1065–1073. Greece, June 26-July 1.

Duan, M.Y., Fu, B.W., Wan, D.C., 2016b. The effect of top tension on VIV model analysis of a vertical flexible riser[C]. In: Proceedings of the Second Conference of Global Chinese Scholars on Hydrodynamics, Nov. 11-14, pp. 455–460. Wuxi, China.

Duan, M.Y., Zou, L., Wan, D.C., 2017. Numerical simulations of vortex-induced vibrations of a flexible riser with different aspect ratiosin uniform and shear currents [J]. J. Hydrodyn. Ser. B 29 (6), 1010–1022.

Duan, M.Y., Zou, L., Wan, D.C., 2018. Numerical analysis of multi-modal vibrations of a vertical riser in step currents[J]. Ocean Eng. 152, 428–442.

Fu, B.W., Duan, M.Y., Wan, D.C., 2016. Effect of mass ratio on the vortex-induced vibrations of a top tensioned riser[C]. In: Proceedings of the Second Conference of Global Chinese Scholars on Hydrodynamics, November 11-14, pp. 431–435. Wuxi, China.

Fu, B.W., Zou, L., Wan, D.C., 2017. Numerical study on the effect of current profiles on vortex-induced vibrations in a top-tension riser[J]. J. Mar. Sci. Appl. 16, 473–479.

Fu, B.W., Wan, D.C., 2017. Numerical study of a vertical tension riser excited at the top end[J]. J. Ocean Eng. Sci. 2, 268–278.

Fu, B.W., Zou, L., Wan, D.C., 2018. Numerical study of vortex-induced vibrations of a flexible cylinder in an oscillatory flow[J]. J. Fluid Struct. 77, 170–181.

Fu, S.X., Wang, J.G., Baarholm, R., et al., 2013. VIV of flexible cylinder in oscillatory flow [C]. In: International Conference on Offshore Mechanics and Arctic Engineering, OMAE, June 9–14. Nantes, France, OMAE2013-10348.

Gabbai, R.D., Benaroya, H., 2005. An overview of modeling and experiments of vortex-induced vibration of circular cylinders[J]. J. Sound Vib. 282 (3–5), 575–616.

Gedikli, E.D., Dahl, J.M., 2017. Mode excitation hysteresis of a flexible cylinder undergoing vortex-induced vibrations[J]. J. Fluid Struct. 69 (October 2016), 308–322.

Holmes, S., Oakley, O.H., Constantinides, Y., 2006. Simulation of riser VIV using fully three dimensional CFD simulations[C]. In: International Conference on Offshore Mechanics and Arctic Engineering, OMAE, June 4–9. Hamburg, Germany, OMAE2006-92124.

Huang, K., Chen, H., Chen, C.R., 2007. Riser VIV analysis by a CFD approach[C]. In: Proceedings of the Seventeenth International Ocean and Polar Engineering Conference, pp. 2722–2729. Lisbon, Portugal, July 1-6.

Huang, K., Chen, C.R., 2007. Time-domain simulation of riser VIV in sheared current[C]. In: International Conference on Offshore Mechanics and Arctic Engineering, OMAE, June 10–15. San Diego, California, USA, OMAE2007-29363.

Huang, X.D., Zhang, H., Wang, X.S., 2009. An overview on the study of vortex-induced vibration of marine riser[J]. J. Mar. Sci. 27, 95–101, 04.

Huera Huarte, F.J., 2006. Multi-mode Vortex-Induced Vibrations of a Flexible Circular Cylinder[D]. PhD thesis. the University of London.

Lehn, E., 2003. VIV Suppression Tests on High L/D Flexible Cylinders. Norwegian Marine Technology Research Institute, Trondheim, Norway.

Lie, H., Kaasen, K.E., 2006. Modal analysis of measurements from a large-scale VIV model test of a riser in linearly sheared flow[J]. J. Fluid Struct. 22 (4), 557–575.

Meneghini, J.R., Saltara, F., Fregonesi, R.D.A., et al., 2004. Numerical simulations of VIV on long flexible cylinders immersed in complex flow fields[J]. Eur. J. Mech. B Fluid 23 (1), 51–63.

Menter, F.R., 1993. Zonal Two Equation K-ω Turbulence Models for Aerodynamic flows [R]. AIAA-93-2906.

Sanaati, B., Kato, N., 2012. A study on the effects of axial stiffness and pre-tension on VIV dynamics of a flexible cylinder in uniform cross-flow[J]. Appl. Ocean Res. 37, 198–210.

Sarpkaya, T., 1979. Vortex-induced oscillations[J]. J. Appl. Mech. 46, 241–258.

Sarpkaya, T., 2004. A critical review of the intrinsic nature of VIV[J]. Fluid Mech. Appl. 75, 159–161.

Song, J.N., Lu, L., Teng, B., et al., 2011. Laboratory tests of vortex-induced vibrations of a long flexible riser pipe subjected to uniform flow[J]. Ocean Eng. 38 (11–12), 1308–1322.

Song, L., Fu, S., Dai, S., et al., 2016. Distribution of drag force coefficient along a flexible riser undergoing VIV in sheared flow[J]. Ocean Eng. 126, 1–11.

Tang, Y.G., 2002. Advanced Structural dynamics[M]. Tianjin University Press, Tianjin.

Tognarelli, M.A., Slocum, S.T., Frank, W.R., et al., 2004. VIV Response of a Long Flexible Cylinder in Uniform and Linearly Sheared Currents[C]. Offshore Technology Conference, Houston, Texas, USA, p. 16338. May 3-6.

Trim, A.D., Braaten, H., Lie, H., et al., 2005. Experimental investigation of vortex-induced vibration of long marine risers[J]. J. Fluid Struct. 21, 335–361.

Wan, D.C., Duan, M.Y., 2017. A recent review of numerical studies on vortex-induced vibrations of long slender flexible risers in Deep Sea[J]. Chin. Q. Mech. 38, 179–196, 02.

Wang, E., Xiao, Q., 2016. Numerical simulation of vortex-induced vibration of a vertical riser in uniform and linearly sheared currents[J]. Ocean Eng. 121, 492–515.

Willden, R.H.J., Graham, J.M.R., 2001. Numerical prediction of VIV on long flexible circular cylinders[J]. J. Fluid Struct. 15 (3–4), 659–669.

Willden, R.H.J., Graham, J.M.R., 2004. Multi-modal Vortex-Induced Vibrations of a vertical riser pipe subject to a uniform current profile[J]. Eur. J. Mech. B Fluid 23 (1), 209–218.

Williamson, C.H.K., Govardhan, R., 2004. Vortex-induced vibrations[J]. Annu. Rev. Fluid Mech. 36, 413–455.

Wu, X., Ge, F., Hong, Y., 2012. A review of recent studies on vortex-induced vibrations of long slender cylinders[J]. J. Fluid Struct. 28, 292–308.

Yamamoto, C.T., Meneghini, J.R., Saltara, F., et al., 2004. Numerical simulations of vortex-induced vibration on flexible cylinders[J]. J. Fluid Struct. 19 (4), 467–489.